Decomposition Behavior of M(DPM)$_n$ (DPM = 2,2,6,6-Tetramethyl-3,5-heptanedionato; n = 2, 3, 4)

Yinzhu Jiang, Mingfei Liu, Yanyan Wang, Haizheng Song, Jianfeng Gao,* and Guangyao Meng

USTC Laboratory for Solid State Chemistry & Inorganic Membranes, Department of Materials Science and Engineering, University of Science and Technology of China (USTC), Hefei, 230026, People's Republic of China

Received: June 27, 2006; In Final Form: October 3, 2006

The decomposition behavior of M(DPM)$_n$ (DPM = 2,2,6,6-tetramethyl-3,5-heptanedionato; M = Sr, Ba, Cu, Sm, Y, Gd, La, Pr, Fe, Co, Cr, Mn, Ce, Zr; n = 2−4) was studied in detail with infrared spectroscopy and mass spectrometry. The results indicated that the chemical bonds in these compounds dissociate generally following the sequence of C−O > M−O > C−C(CH$_3$)$_3$ > C−C and C−H at elevated temperatures. The decomposition processes of M(DPM)$_n$ are strongly influenced by the coordination number and central metal ion radius. In addition, the decomposed products, in air atmosphere, varied from metal oxides to metal carbonates associated with different M(DPM)$_n$.

1. Introduction

Metal−organic chemical vapor deposition (MOCVD), classified according to the use of metallorganics as precursors, is a well-established, versatile, and widely applied method for fabricating technologically important thin films, ranging from metals to semiconductors, insulators, and superconductors with tailored properties.[1−3] In general, metallorganic precursors possess lower decomposition or pyrolysis temperatures than halides, hydrides, or halohydrides. Thus, these advantages enable the MOCVD process to occur at a lower deposition temperature than conventional chemical vapor deposition (CVD), which generally uses halides or hydrides as precursors.[4]

There are three kinds of metallorganic precursors utilized commonly in MOCVD processes: metal β-diketonates, metal alkoxides, and metal alkyls. Metal β-diketonates have been widely applied in fabrication of electroceramic oxides films, such as high-T_c superconductors, ferromagnetics, ferroelectrics, conducting oxide layers, electrochemical devices, high-k dielectrics, giant magnetoresistant (GMR) oxides, buffer layers, and alloy thin films.[1,5] β-Diketonate complexes used mainly include M(DPM)$_n$ (DPM = dipivaloylmethanate = 2,2,6,6-tetramethyl-3,5-heptanedionato), M(ACAC)$_n$ (ACAC = 2,4-pentanedione),[6] M(HFA)$_n$ (HFA = 1,1,1,5,5,5-hexafluoropentane-2,4-dionate),[7] M(DFHD)$_n$ (DFHD = 1,1,1,2,2,6,6,7,7,7-decafluoro-3,5-heptanedione),[3] et al. In comparison with the other kinds of metallorganic precursors, one of the advantages of metal β-diketonates is that their physical and chemical properties can be altered by "tailoring" the β-diketonate group.[1] Among these β-diketonate complexes, chelates with large steric hindrance ligands, such as M(DPM)$_n$, possess somewhat lower volatility than ones with fluorine. However, the latter is always expensive and produces toxic gas, which may contaminate the as-deposited films. Up to today, M(DPM)$_n$, nontoxic, nonfluorinated and environmentally benign compounds with sufficient volatility and stability are still extensively used in preparing many kinds of materials such as YBCO, CYO, SCYO, YSZ, SDC, and Pd−Pa alloy.[1,8−10]

Knowledge of the decomposition mechanism of metal complexes, particularly the sequence of the bond dissociation in the ligand, is of great importance for two reasons. First, it could provide basic information required to guide us in designing new metallorganic compounds by modifying the primary ligand structures to improve its physical properties and/or decomposition behavior. For instance, in Ba(DPM)$_2$ and Sr(DPM)$_2$, H$_2$O can coordinate to the highly positively charged metal center to form oligomeric oxygen/hydroxide bridged structures, such as Ba$_5$(DPM)$_9$(OH)$_3$H$_2$O and Sr$_2$(DPM)$_3$.[11] In this case, the introduction of fluorine and/or bulky ligand groups into the β-diketonate ligand reduces the net positive charge on the metal center, rendering the compound less sensitive to O$_2$/H$_2$O. Alternatively, the metal center can be saturated with a polydentate coordinating ligand, such as polyethers (CH$_3$O(CH$_2$CH$_2$O)$_n$CH$_3$). These form relatively stable complexes with fluorinated β-diketonates of the type M(hfac)$_2$(polyether) (M = Ba, Sr, Ca; polyether = tetraglyme, triglyme),[12] which have higher vapor pressures and higher ambient stabilities than M(DPM)$_2$ complexes.

Second, the information about precursor decomposition behavior would guide us in optimizing MOCVD process conditions for obtaining a film of desired properties. Examples are Mn(DPM)$_3$ and La(DPM)$_3$, of which Nakamura et al. studied the decomposition mechanism through spectroscopic absorption spectroscopy.[13−15] Meanwhile, the results effectively guide the deposition of lanthanum oxide films and manganese oxide films in a liquid delivery MOCVD process.

In the present study, the decomposition behavior of a series of tris-, bis-, and tetra(dipivaloylmethanate) metal chelates, where the metals complexed were Sr, Ba, Cu, Sm, Y, Gd, La, Pr, Fe, Co, Cr, Mn, Ce, and Zr, were systematically studied by infrared spectroscopy and mass spectrometry. Their possible decomposition mechanisms and influencing factors were proposed and discussed.

* Corresponding author. Telephone: +86-551-3601700. Fax: +86-551-3607627. E-mail: jfgao@ustc.edu.cn.

10.1021/jp064010j CCC: $33.50 © 2006 American Chemical Society
Published on Web 11/24/2006

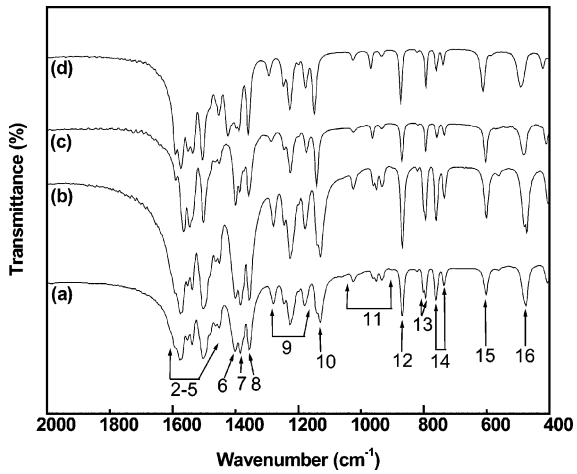

Figure 1. IR spectra of $M(DPM)_n$ at room temperature: (a) $Sm(DPM)_3$, (b) $Pr(DPM)_3$, (c) $Ce(DPM)_4$, and (d) $Zr(DPM)_4$.

2. Experimental Section

Some $M(DPM)_n$ (M = Ba, Sr, Gd, Ce) samples were purchased from Strem; other $M(DPM)_n$ (M = Pr, Mn, Fe, Cr, Co, Y, and Sm) samples were synthesized in-house, using corresponding inorganic salts and HDPM (Strem) as starting materials. The reaction was fulfilled in 50% ethanol/aqueous mixture solution,[16] where the favored pH value was controlled by sodium hydroxide addition. These $M(DPM)_n$ precipitates were quickly filtered off, dried, and purified by recrystallization from toluene. Final $M(DPM)_n$ chelates were dried by P_2O_5 in a desiccator. All the samples were verified to be of high purity by the former characterization of carbon and hydrogen elementary analysis (VARIO ELIII), metal atomic absorption spectrophotometric analysis (Perkin-Elmer 3100), and nuclear magnetic resonance (^{1}H NMR, AV300) for a sample dissolved in $CDCl_3$.

To investigate the mechanisms of the bond dissociation in $M(DPM)_n$ (M = Sm, Ce, Zr, Pr), we observed changes in the Fourier transform infrared (FTIR) peak intensity while the sample was heated to a certain temperature. The FTIR spectrum was recorded from 400 to 4000 cm^{-1} using the Bruker FT-IR spectrometer, Model Vector-22. The sample was mixed with KBr powder, pressed into a self-supporting disk, and then placed at the center of the IR cell for experiments. In addition, a mass spectrometer (Agilent 6890/Micromass GCT-MS) was used to obtain more explicit and idiographic oligomerization mechanisms of these metal complex. The cracking patterns of $M(DPM)_n$ and the mass signal changes were monitored as the sample was heated in a vacuum at the rate of 10 °C/min from 30 to 400 °C. The samples were ionized by the electron impact (EI) method within the scanned mass range of 1−800 *m*/*z*.

3. Results and Discussion

3.1. FTIR Spectra. To explore the processes of the bond dissociation of the mentioned $M(DPM)_n$, the samples were heated to different temperatures and the changes in the FTIR peak intensity were recorded. Figure 1 shows the FTIR spectra of fresh $M(DPM)_n$ (M = Sm, Ce, Zr, Pr) at room temperature. All the complexes show similar FTIR spectra, which suggests that they possess the same ligand DPM. Table 1 lists the observed wavenumber with band assignments of these complexes and other $M(DPM)_n$ chelates. These results are inconsistent with those of other reported $M(DPM)_n$.[13,17] In the IR absorption spectra of fresh samples, the peaks numbered 2, 3, and 4 represent the stretching vibrational mode of C−O, C−C, and the bending vibrational mode of C−H in the ring structure,

TABLE 1: Observed Wavenumber and Band Assignments of the $M(DPM)_n$

		wavenumber (cm^{-1})								
peak no.	predominant mode	$Ce(DPM)_4$	$Gd(DPM)_3$	$Y(DPM)_3$	$Zr(DPM)_4$	$Sm(DPM)_3$	$Pr(DPM)_3$	$Mn(DPM)_3$	$Fe(DPM)_3$	$Co(DPM)_3$
1	$\gamma(CH_3)$	2961, 2867	2962, 2868	2958, 2866	2962, 2867	2960, 2865	2962, 2868	2960, 2866	2964, 2866	2959, 2867
2	γ(C−O)	1593,1565	1578	1597, 1572	1591, 1574	1577	1574	1592, 1569	1593, 1562	1575, 1561
3	γ(C−C)	1546	1554, 1539	1556	1550, 1535	1552, 1538	1553, 1538	1548, 1528	1546	1525
4	γ(C−O) + γ(C−C) + δ(C−H)	1502	1504	1508	1504	1504	1502	1496	1506	1494
5	γ(C−C) + δ(C−H)	1453	1464, 1452	1452	1452	1451	1451	1452	1453	1456
6	$\delta_d(CH_3)$	1399	1404	1410	1408, 1398	1401	1400	1401	1396	1398
7	γ(M−O) + γ(C−O)	1387	1385	1389	1388	1384	1384	1387	1372	1385
8	$\delta_s(CH_3)$	1358	1356	1360	1360	1356	1356	1358	1353	1358
9	γ[C−(CH_3)] + δ(C−C)	1286, 1245, 1225, 1174	1281, 1246, 1227, 1180	1290, 1248, 1228, 1198, 1174	1292, 1246, 1227, 1200, 1178	1279, 1226, 1180	1279, 1245, 1226, 1179	1285, 1246, 1223, 1175	1292, 1251, 1227, 1177	1245, 1228, 1178
10	γ[C−$C(CH_3)_3$] + δ(C−H)	1142	1132	1144	1147	1130	1129	1135	1144	1149
11	$\rho_r(CH_3)$	1023, 964, 932	1024, 953, 933	1024, 964, 935	1026, 968, 935	1024, 951, 934	1025, 951, 933	1024, 958, 935	1024, 961, 937	1026, 968, 936
12	γ[C−$C(CH_3)_3$] + γ(C−O)	870	870	872	874	869	868	871	872	876
13	π(C−H)	812, 794	802, 795	820, 798	822, 793	794	821, 794	792	820, 794	824, 784
14	γ[C−$C(CH_3)_3$] + γ(C−C−O) + γ(M−O)	759, 735	762, 737	766, 737	760, 739	761, 736	761, 735	759, 739	760, 739	753, 714
15	ring + γ(M−O)	603	603	611	613	602	601	640	623	662
16	γ(M−O)	482	476	490	494	475	474	506, 479	502, 480	517, 457

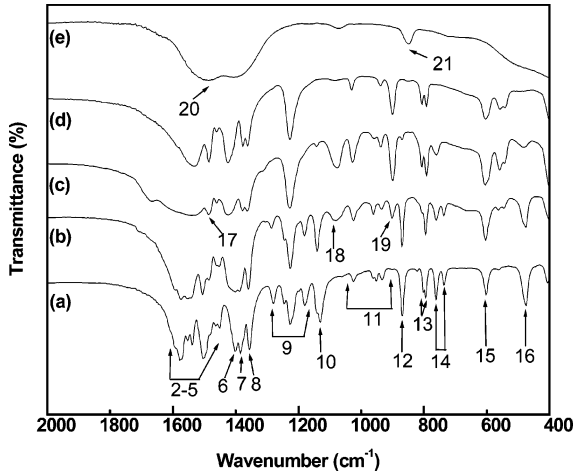

Figure 2. IR spectra of Sm(DPM)$_3$ at room temperature (a) and preheated at various temperatures: (b) 200, (c) 270, (d) 325, and (e) 400 °C.

which contribute to the tautomeric equilibrium of the keto and enol forms. The peaks numbered 15 and 16 are due to the stretching mode of the M−O bond. These results can be used to identify these complexes.[18] A broad peak ranging from 3300 to 3600 cm^{-1} in each spectrum represents the O−H vibrational mode in H_2O, which was adsorbed by the sample and/or KBr during the preparation of IR sample.

Spectra b, c, d, and e in Figure 2show the IR spectra of Sm(DPM)$_3$ heated at four different temperatures: 200, 270, 325, and 400 °C, respectively.[19] These IR results indicate that the chemical bonds in Sm(DPM)$_3$ decompose in sequence when the sample is heated. It can be seen that the intensities of the peaks corresponding to the C−O bond are greatly weakened as the temperature rises to 200 °C, and disappear eventually when the sample is heated to 270 °C. Accompanying the disappearance of the peak at 1573 cm^{-1} for the C−O bond, a new peak (numbered 17) appears at 1486 cm^{-1} above 270 °C, representing the stretching mode of CO_3^{2-}, and maintains its intensity up to 400 °C. This result suggests the generation of $Sm_2(CO_3)_3$. The intensity of the peak for the Sm−O bond is reduced continuously from low temperatures up to 325 °C, indicating that the chemical bond between the Sm ion and DPM ligand is also unstable, similar to the Sr−O bond in Sr(DPM)$_2$.

The peaks between 1100 and 1300 cm^{-1} and those between 700 and 900 cm^{-1}, corresponding to the C−C(CH$_3$)$_3$ bond, decrease slowly above 200 °C, and two new peaks (numbered 18 and 19) assigned to the new vibrational modes of CH_3 appear at 1079 and 901 cm^{-1}. When the bond of C−C(CH$_3$)$_3$ is dissociated partially while the sample is heated at higher temperature, it could be found that the two new peaks go through two stages: (1) while all the peaks for C−C(CH$_3$)$_3$ decrease and the peaks for C−O disappear before 270 °C, the intensity of the two new peaks increases; (2) when the peaks for C−C(CH$_3$)$_3$ disappear partially from 270 °C, we can see the intensity of the two new peaks decreases dramatically, and then disappear at 325 and 400 °C, respectively. This phenomenon may be interpreted as by follows: at the first stage, along with the dissociation of the C−O bond, the ligand structure becomes more flexible and therefore it is easier for the vibration of CH_3; at the second stage, the bond of C−C(CH$_3$)$_3$ is dissociated partially, and the amount of the CH_3 reduces, too, which results in the decrease of the two new peaks.

By reason of dissociation of the C−O bond at relatively low temperature, the ligand ring opens so that the ligand is attached only at one end. Hence the ligand structure becomes more

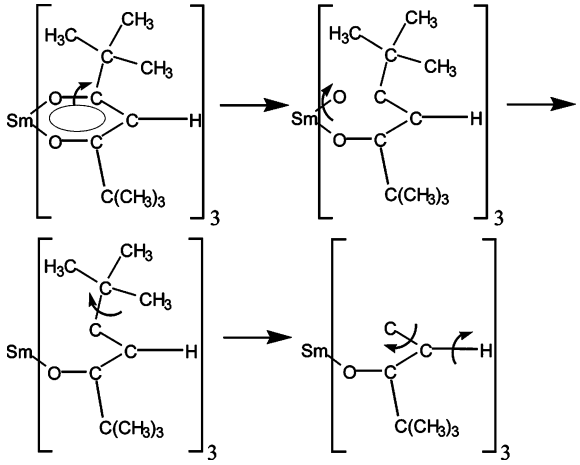

Figure 3. Schematic diagram of the proposed thermal decomposition process of Sm(DPM)$_3$ in air.

TABLE 2: Decomposition Temperatures and Decomposed Products of M(DPM)$_n$ (M = Pr, Sm, Ce, Zr)

complex	decomposition temp[a] (°C)	decomposed products
Pr(DPM)$_3$	∼280	praseodymium oxide and praseodymium oxide carbonate
Sm(DPM)$_3$	∼200	$Sm_2(CO_3)_3$ and Sm_2O_3
Ce(DPM)$_4$	∼220	CeO_2
Zr(DPM)$_4$	∼260	ZrO_2

[a] According to IR analysis.

flexible, resulting in an increase of the coupling of C−C vibrational modes, and then the intensity of the peaks for C−C bonds enhances at around 1540 cm^{-1} as observed from 270 to 325 °C, which was also reported by Ryu et al.[17] The peaks for C−C disappear up to 400 °C due to excessive temperature. For a similar reason, the peak intensity for C−H increases from 200 to 270 °C, then decreases from 270 °C, and finally disappears at 400 °C.

The IR results indicate that Sm(DPM)$_3$ dissociates in sequence heated in air. The C−O and the Sm−O bonds decompose easily at relatively low temperature, and then the C−C(CH$_3$)$_3$ bond decomposes. The C−H and C−C bonds are the most stable, dissociating at a higher temperature. The proposed sequence of the bond dissociation in Sm(DPM)$_3$ is described schematically in Figure 3.

All chemical bonds of organic groups dissociate completely at 400 °C, and two broad peaks (numbered 20 and 21) at 1486 cm^{-1} and about 480 cm^{-1} corresponding to the stretching modes of $Sm_2(CO_3)_3$ and Sm_2O_3, respectively, indicate that the residue of the complex decomposed in air is a mixture of samarium oxide and samaric carbonate.

A similar evolution of the bond dissociation is demonstrated through the study on the IR spectra of Zr(DPM)$_4$, Ce(DPM)$_4$, and Pr(DPM)$_3$ heated at different temperatures.[18] However, each of the complexes exhibits different decomposition temperatures and decomposed products at elevated temperatures in air (Table 2). It should be pointed out that the decomposition temperatures determined by IR analysis are generally less than those determined by differential thermal analysis (DTA) owing to heat relaxation.[19] For the sake of optimal conditions, the addition of extra oxidant, such as oxygen, is needed when MOCVD is applied for deposition of metal oxides films using M(DPM)$_n$ as precursors. The added oxygen will promote the complete decomposition of the precursors, as well as prevent carbon and/or other impurities from remaining in the films. Meanwhile,

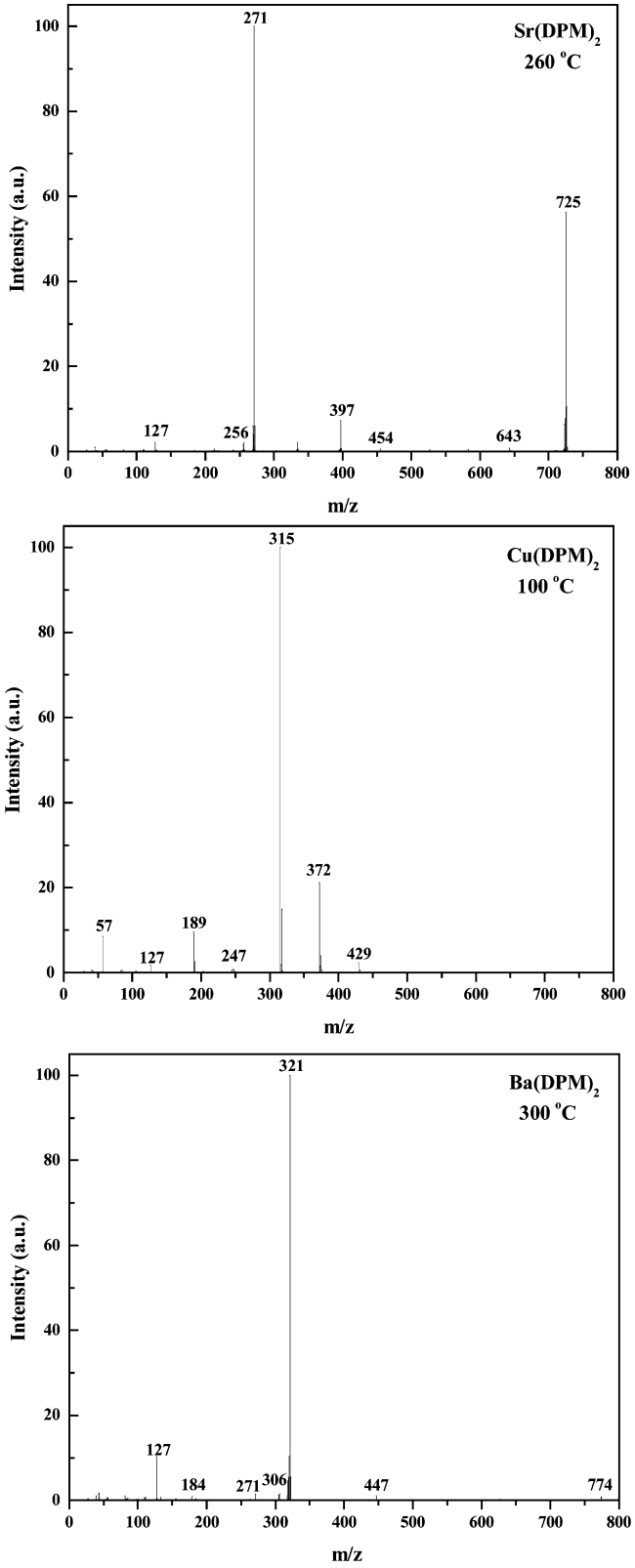

Figure 4. Typical mass spectrum of $M(DPM)_2$ (M = Sr, Ba, and Cu).

the deposition should be processed in the system without water vapor and CO_2, so as to prevent the formation of carbonate byproduct.

3.2. Mass Spectroscopic Analysis. Mass spectrometry is one of the effective tools for the investigation of the dissociation mechanisms of chemical bonds in an organic compound. In the present experiments, mass spectrometry was applied for examining the dissociation processes of $M(DPM)_n$ and the properties

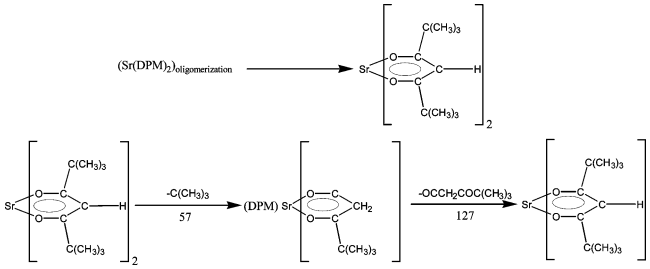

Figure 5. Possible decomposition mechanism of $Sr(DPM)_2$.

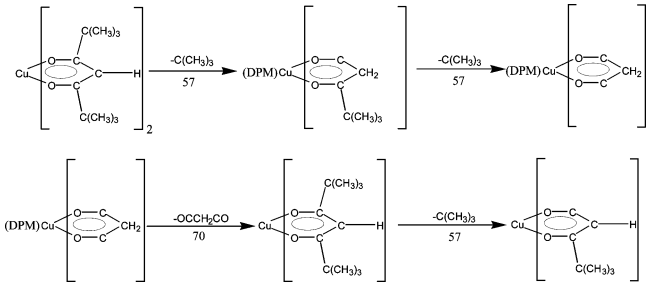

Figure 6. Possible decomposition mechanism of $Cu(DPM)_2$.

of ionized fragments released from the chelates while the sample is heated.

3.2.1. M(DPM)$_2$ (M = Sr, Ba, Cu). Figure 4 shows the prevailing mass fragments of $M(DPM)_2$ (M = Sr, Ba, and Cu). Each of the complexes exhibits different decomposition behaviors.

In the mass spectra of the compounds of $Sr(DPM)_2$ and $Ba(DPM)_2$ could be found peaks with *m*/*z* exceeding 454 and 504 (respective molecular weights of $Sr(DPM)_2$ and $Ba(DPM)_2$). The results have been noted earlier elsewhere and clearly ascribed to the oligomerization of $Sr(DPM)_2$ and $Ba(DPM)_2$. However, the peaks at *m*/*z* above 800 in the mass spectrum of $Ba(DPM)_2$ could not be detected under our current experimental conditions, although they do exist in the process of oligomerization of $Ba(DPM)_2$, e.g., $^+Ba_4(DPM)_7$ and $^+Ba_3(DPM)_5$.[12] The other major peaks of the various fragments of $Sr(DPM)_2$ are as follows: The base peak at $m/z = 271$ corresponds to $^+Sr(DPM)$. The peaks at $m/z = 397$, 256, and 127 correspond to $^+OCCH_2COC(CH_3)_3Sr(DPM)$, $^+C(CH_3)_2OCCHCOC(CH_3)_3Sr$, and $^+OCCH_2COC(CH_3)_3$. The peaks in the mass spectrum of $Ba(DPM)_2$ is similar to those of $Sr(DPM)_2$, which indicates similar decomposition behavior as shown in Figure 5.

In the mass cracking patterns of $Cu(DPM)_2$, the parent peak, i.e., $^+Cu(DPM)_2$, $m/z = 429$, corresponds to the molecular weight of the complex and thus confirms the formation of the complex. At the same time, the absence of peaks with *m*/*z* exceeding 429 (molecular weight of the compound) is indicative of the monomer composition of the gas phase. However, Turnispeed et al. found the oligomerization of $Cu(DPM)_2$ under their experimental conditions, e.g., $Cu_2(DPM)_2$ and $Cu_2(DPM)_3$.[12] The diversity may be due to the different synthesis methods of the $Cu(DPM)_2$ source. The other major peaks at $m/z = 372$, 315, 246, 189, 127, and 57 correspond to $^+Cu(DPM)_2$, $^+OCCH_2COC(CH_3)_3Cu(DPM)$, $^+OCCH_2COCCu(DPM)$, $^+Cu(DPM)$, $^+OCCH_2COC(CH_3)_3Cu$, $^+OCCH_2COC(CH_3)_3$, and $^+C(CH_3)_3$, respectively. These mass fragments reveal the possible process of decomposition in a vacuum, which is described in Figure 6: In the beginning, the C−O bond dissociates by heating and the ligand structure becomes more flexible, resulting in the detachment of the two $-C(CH_3)_3$ groups successively. Afterward, the residual $-OCCH_2CO-$ group dissociates from the central metal atom, leading to the formation of $^+Cu(DPM)$.

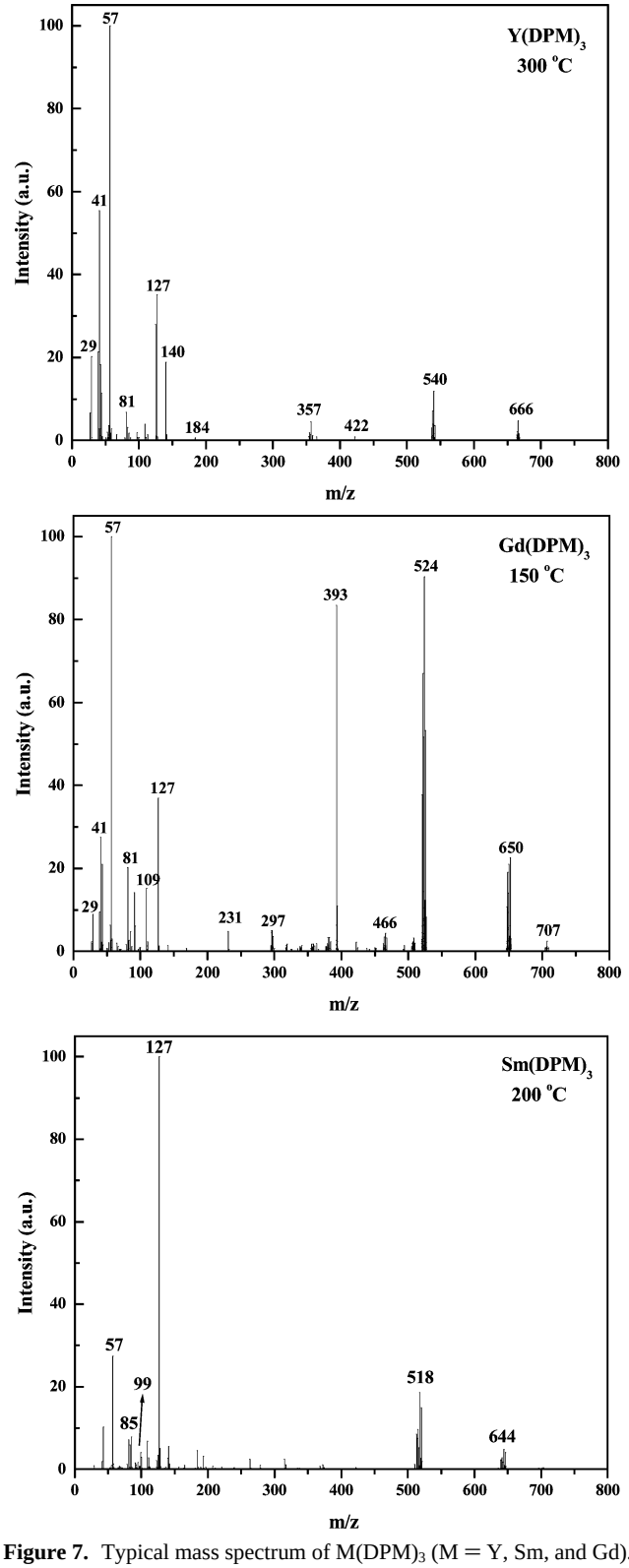

Figure 7. Typical mass spectrum of $M(DPM)_3$ (M = Y, Sm, and Gd).

3.2.2. $M(DPM)_3$ (M = Y, Sm, Gd, La, Pr). Figure 7 shows typical mass spectra for $M(DPM)_3$ (M = Sm, Y, Gd), which exhibit similar fragment distribution. For the mass spectrum of $Sm(DPM)_3$, six major peaks of highest mass are observed at m/z = 644, 518, 127, 99, 85, and 57, corresponding to $^+OCCH_2COC(CH_3)_3Sm(DPM)_2$, $^+Sm(DPM)_2$, $^+OCCH_2COC(CH_3)_3$, $^+CH_2COC(CH_3)_3$, $^+COC(CH_3)_3$, and $^+C(CH_3)_3$, respectively. Based on these mass fragments, a possible process of the decomposition was proposed in Figure 8. First, the $-CC(CH_3)_3$ group detaches from DPM ligand first, and then the $-OCCH_2COC(CH_3)_3$ group in the same DPM ligand detaches. The mechanism is consistent with the IR analysis: the C−O bond dissociates in the beginning by heating and the ligand structure becomes more flexible, resulting in the detachment of the $-CC(CH_3)_3$. The strongest peaks appear at m/z = 127 and 57, indicating that this process is dominant.

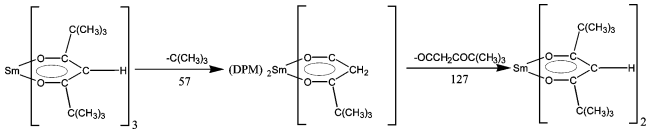

Figure 8. Possible decomposition mechanism of $Sm(DPM)_3$.

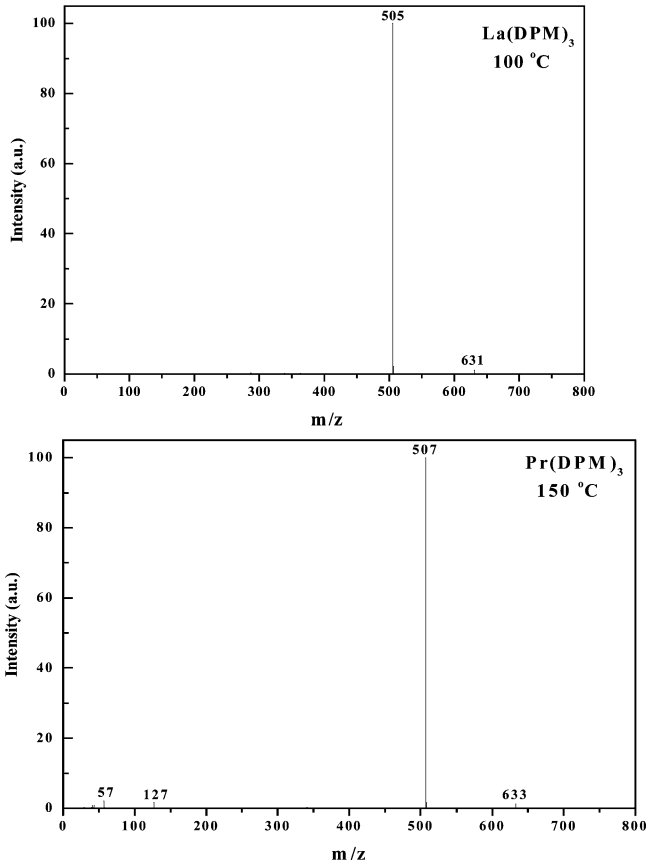

Figure 9. Typical mass spectrum of $M(DPM)_3$ (M = La and Pr).

The mass cracking patterns of $La(DPM)_3$ and $Pr(DPM)_3$ are given in Figure 9. In comparison with the above spectra of $M(DPM)_3$ (M = Sm, Y, Gd), the mass fragment peaks are obviously fewer, and the base peaks at m/z = 507 and 505 correspond to $^+M(DPM)_2$ (M = La, Pr).

3.2.3. $M(DPM)_3$ (M = Transition Metals, Cr, Mn, Co, Fe). Figure 10 shows the total ion current of the mass signal of $Mn(DPM)_3$ and prevailing mass fragments at four different temperature regions. In the low-temperature region (T < 203 °C), five major peaks of the highest mass are observed at m/z = 421, 364, 238, 127, and 57, corresponding to $^+Mn(DPM)_2$, $^+OCCHCOC(CH_3)_3Mn(DPM)$, $^+Mn(DPM)$, $^+OCCH_2COC(CH_3)_3$, and $^+C(CH_3)_3$, respectively. These mass fragments reveal the possible process of decomposition under vacuum (Figure 11). In the beginning, one of the DPM groups detaches from the Mn atom, leading to the formation of $^+Mn(DPM)_2$ (m/z = 421); then the $-C(CH_3)_3$ and the $-OCCH_2COC(CH_3)_3$ groups dissociate in sequence partially from the DPM ligand of $^+Mn(DPM)_2$. The similar dissociation process is also verified in the investigation of $Cr(DPM)_3$, $Co(DPM)_3$, and $Fe(DPM)_3$, as shown in Figure 12.

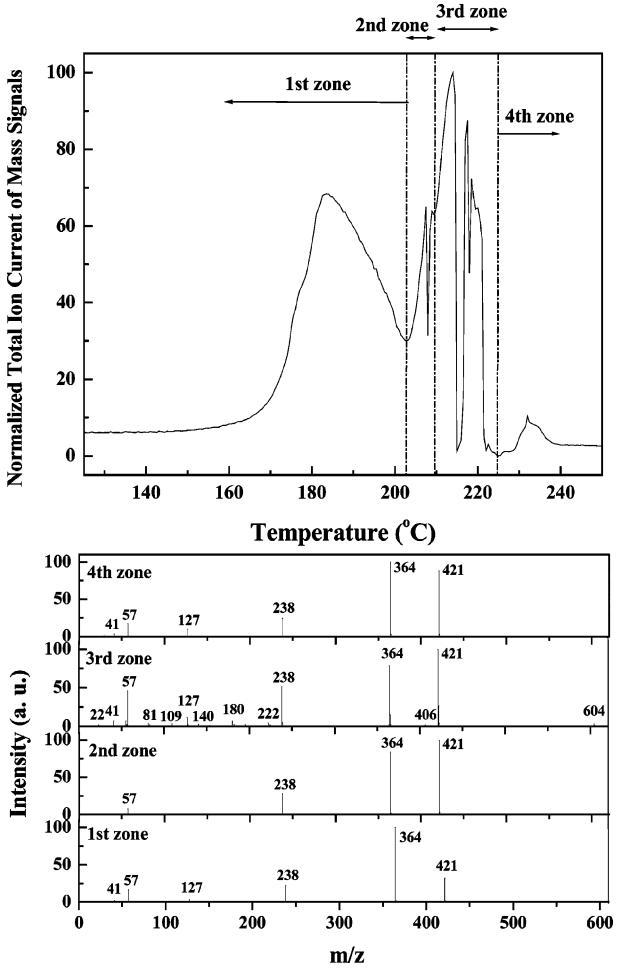

Figure 10. (a, top) Changes in total ion current of mass signals of $Mn(DPM)_3$ with temperature. (b−e, bottom) Mass cracking patterns of $Mn(DPM)_3$ in four temperature regions: (b, first zone) 125 °C < *T* < 203 °C, (c, second zone) 203 °C < *T* < 210 °C, (d, third zone) 210 °C < *T* < 225 °C, and (e, fourth zone) 225 °C < *T* < 250 °C.

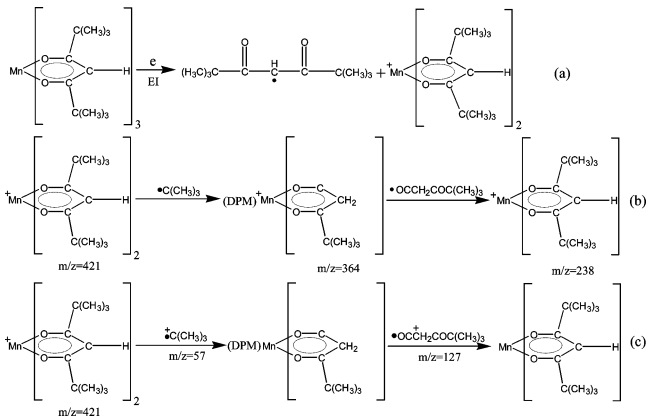

Figure 11. Schematic diagram of the proposed decomposition mechanism of $Mn(DPM)_3$ under vacuum.

On the whole, the bond dissociation process in $Mn(DPM)_3$ (Figure 11b,c) is similar to the above results and reported ones of other $M(DPM)_n$:[17−19] the C−O bond dissociates by heating and the ligand structure becomes more flexible, resulting in the detachment of the $-CC(CH_3)_3$ and $-OCCH_2COC(CH_3)_3$ successively. However, different from the above results of $M(DPM)_n$, one of the DPM groups will detach from $Mn(DPM)_3$ (Figure 11a) in advance of the following dissociation (Figure 11b,c).

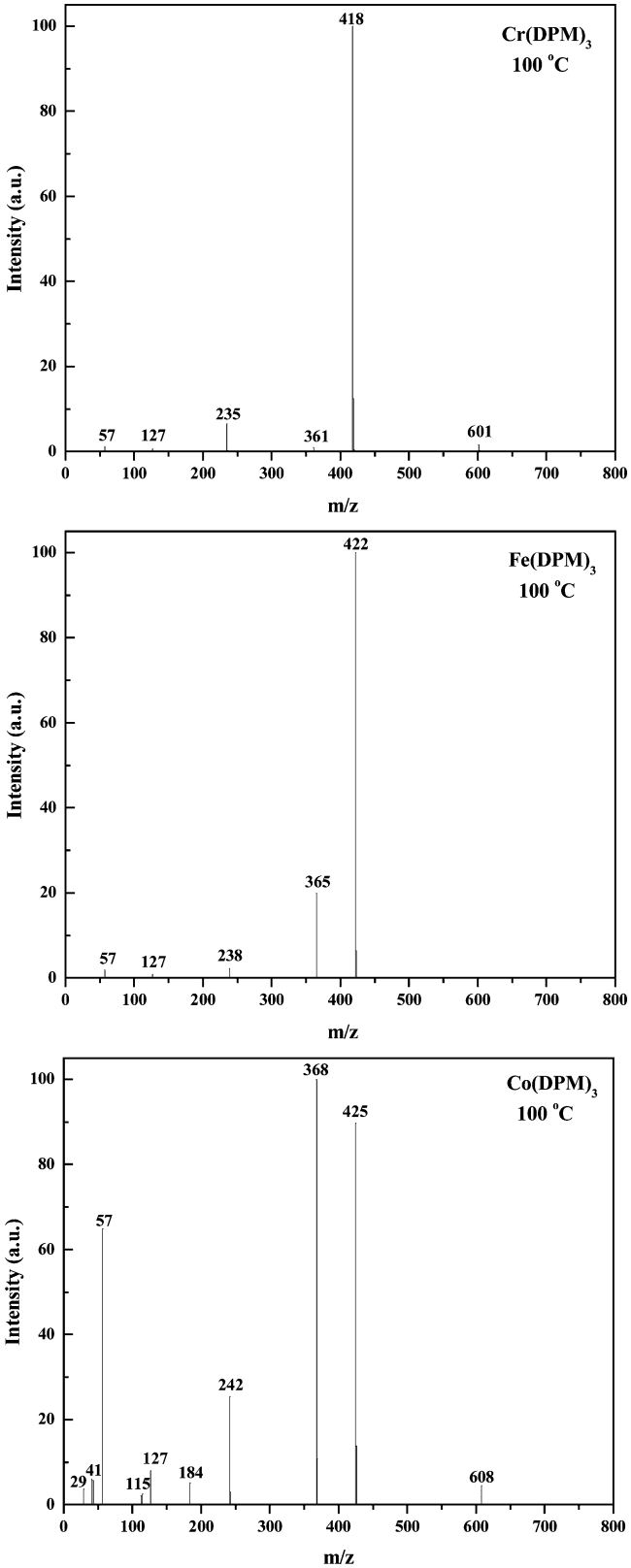

Figure 12. Typical mass spectrum of $M(DPM)_3$ (M = Cr, Co, and Fe).

When the temperature increases to the second zone (203−210 °C; see Figure 10), the intensity of the peak at $m/z = 421$ increases to be the strongest peak, indicating that the $^+Mn(DPM)_2$ fragment becomes uppermost among all the fragments. The change may be interpreted by the following reasons: when the temperature is above 203 °C, the complex largely vaporizes, leading to the acceleration of reaction a (Figure 11a) and then

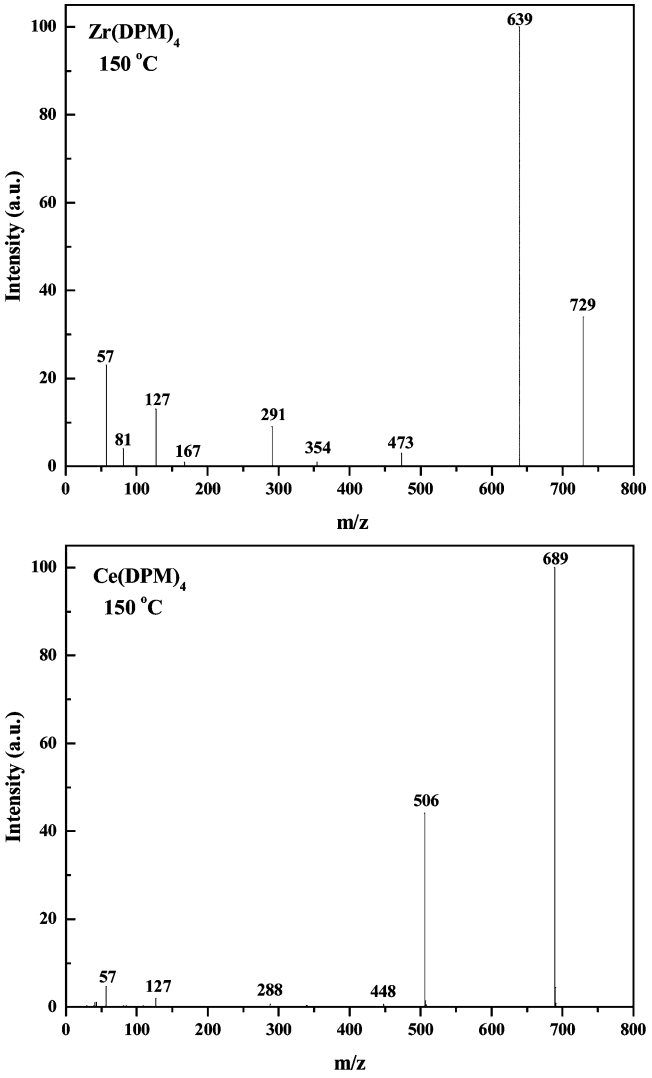

Figure 13. Typical mass spectrum of M(DPM)$_4$ (M = Zr and Ce).

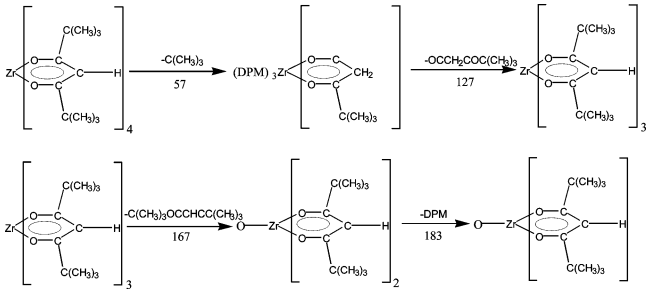

Figure 14. Possible decomposition mechanism of Zr(DPM)$_4$.

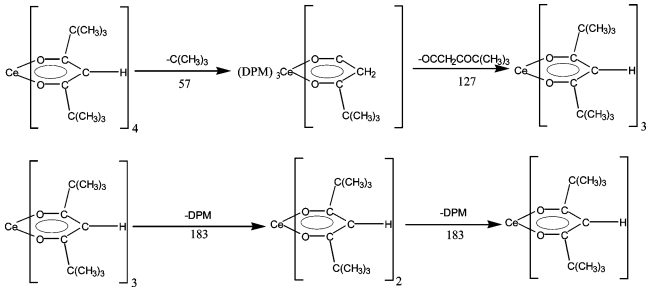

Figure 15. Possible decomposition mechanism of Ce(DPM)$_4$.

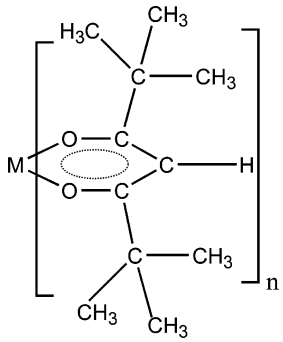

Figure 16. Chemical structure of M(DPM)$_n$.

the vast production of $^+$Mn(DPM)$_2$ fragment. When the temperature increases more, the primary fragments possess lower activation energy and easier dissociation, which lead to the appearance of various dissociation reactions and hence various fragments. The fourth zone (Figure 10) shows the end of the decomposition of Mn(DPM)$_3$.

3.2.4. M(DPM)$_4$ (M = Ce, Zr). Figure 13 shows the mass spectra of tetra(dipivaloylmethanate) metal chelates Zr(DPM)$_4$ and Ce(DPM)$_4$. The peaks at m/z = 127 and 57, which reprensent $^+$OCCH$_2$COC(CH$_3$)$_3$ and $^+$C(CH$_3$)$_3$ fragments, are observed in both spectra. Except for these, the mass spectra of Zr(DPM)$_4$ and Ce(DPM)$_4$ exhibit a great many diversities in the mass fragments. The spectrum for Zr(DPM)$_4$ contains $^+$Zr(DPM)$_3$ (m/z = 640), $^+$Zr(DPM)$_2$O (m/z = 473), and $^+$Zr(DPM)O (m/z = 290), whereas peaks at m/z = 690 and 507, corresponding to $^+$Ce(DPM)$_3$ and $^+$Ce(DPM)$_2$, appear in the mass spectrum of Ce(DPM)$_4$. The results reveal the different possible decomposition behaviors of Zr(DPM)$_4$ and Ce(DPM)$_4$, which are described in Figures 14 and 15, respectively.

3.3. Discussion. In the structure of M(DPM)$_n$ molecule (Figure 16), each metal M atom is spherically surrounded by 2n oxygen atoms from DPM bidentate ligands. Generally, for M(DPM)$_n$ (n > 2), there will be no oligomerization due to a large steric bulk ligand shielding the positively charged metal center and preventing it from increasing its coordination number by forming intermolecular bonds.

It is well-known that the properties of M(DPM)$_n$, especially the decomposition behaviors, are strongly influenced by the coordination number and the molecular structure. For example, in the chemical structure of M(DPM)$_3$, oxygen atoms in DPM groups are bonded with the central metal atom to form C_3 or D_3 symmetry.[20] Their decomposition properties are influenced by two factors: the chemical nature of the central metal ion, such as electronegativity, and the degree of distortion of the frame structure that is related to the radius of the metal ion. Figure 17 illustrates each metal ion radius. When the metal ion radius is larger, for example, Sm (R = 0.96 Å), the frame structure will be normal or expand; therefore there are no high repulsions between the DPM groups, which will result in the detachment of the $-$CC(CH$_3$)$_3$ and $-$OCCH$_2$COC(CH$_3$)$_3$ successively. A similar decomposition mechanism is observed in Y(DPM)$_3$, Gd(DPM)$_3$, La(DPM)$_3$, and Pr(DPM)$_3$. The latter two possess higher metal ion radii, which may hence exhibit somewhat different phenomena in the mass spectra. On the other hand, when the metal ion radius is relatively smaller, such as transition metal Mn^{3+} (R = 0.66 Å), the DPM groups will shrink toward the central metal atom, resulting in higher repulsion between the DPM groups. Therefore, one of the DPM groups will detach directly from the ligand structure. A similar dissociation process is also verified in the investigation of Cr(DPM)$_3$, Co(DPM)$_3$, and Fe(DPM)$_3$, the metal ion radii of which are 0.63, 0.63, and 0.64 Å, respectively. In addition,

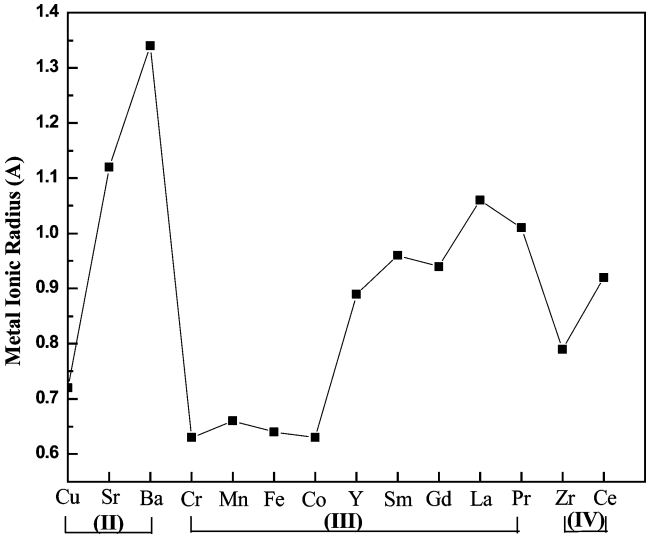

Figure 17. Plot of changes in the metal ion radius.

different electronic structures of metal ions may be the other reason for the variation of the decomposition mechanisms.

4. Summary

A systematic research on the decomposition behavior of $M(DPM)_n$ (DPM = 2,2,6,6-tetramethyl-3,5-heptanedionato; M = Sr, Ba, Cu, Sm, Y, Gd, La, Pr, Fe, Co, Cr, Mn, Ce, Zr; n = 2−4) was provided. The chemical bonds in these compounds begin to dissociate at low temperatures and are sequentially decomposed at elevated temperatures, according to the order of C−O > M−O > C−$C(CH_3)_3$ > C−C and C−H. The decomposed products varied from metal oxides to metal carbonates in air atmosphere. According to mass spectroscopic analysis at elevated temperature, detailed decomposed mechanisms were proposed and classified in term of coordination number and metal ion radius.

Acknowledgment. This work was supported by the National Natural Science Foundation of China under Contract No. 20271047.

References and Notes

(1) Jones, A. C. *Chem. Vap. Deposition* **1998**, *4*, 5.

(2) Mcaleese, J.; Plakatouras, J. C.; Steele, B.C. H. *Thin Solid Films* **1996**, *280*, 152.

(3) Otway, D. J.; Rees, W. S. *Coord. Chem. Rev.* **2000**, *210*, 279.

(4) Choy, K. L. *Prog. Mater. Sci.* **2003**, *48*, 57.

(5) Watson, I. M. *Chem. Vap. Deposition* **1997**, *3*, 9.

(6) Wang, H. B.; Xia, C. R.; Peng, D. K.; Meng, G. Y. *Mater. Lett.* **2000**, *44*, 23.

(7) Artaud, M. C.; Ouchen, F.; Martin, L.; Duchemin, S. *Thin Solid Films* **1998**, *324*, 115.

(8) Reijnen, L.; Feddes, B.; Vredenberg, A. M.; Schoonman, J.; Goossens, A. *J. Phys. Chem. B* **2004**, *108*, 9133.

(9) Jiang, Y. Z.; Song, H. Z.; Ma, Q. L.; Meng, G. Y. *Thin Solid Films* **2006**, *510*, 88.

(10) Iton, K.; Matsumoto, O. *Thin Solid Films* **1999**, *345*, 29.

(11) Timmer, K.; Spee, C. I. M. A.; Mackor, A.; Meinema, H. A.; Spek, A. L.; van Sluis, P. *Inorg. Chim. Acta* **1991**, *190*, 109.

(12) Turnipseed, S. B.; Barkley, R. M.; Sievers, R. E. *Inorg. Chem.* **1991**, *30*, 1164.

(13) Nakamura, T.; Tai, R.; Nishimura, T.; Tachibana, K. *J. Electrochem. Soc.* **2005**, *152*, C584.

(14) Nakamura, T.; Tai, R.; Nishimura, T.; Tachibana, K. *J. Appl. Phys.* **2005**, *97*, 712.

(15) Nakamura, T.; Nishimura, T.; Tai, R.; Tachibana, K. *Mater. Sci. Eng., B* **2005**, *118*, 253.

(16) Hammond, G. S.; Nonhebel, D. C.; Wu, C. S. *Inorg. Chem.* **1963**, *2*, 73.

(17) Ryu, H.; Heo, J. S.; Cho, S.; Chung, C.; Moon, S. H. *J. Electrochem. Soc.* **2000**, *147*, 1130.

(18) Song, H. Z.; Jiang, Y. Z.; Xia, C. R.; Meng, G. Y.; Peng, D. K. *J. Cryst. Growth* **2003**, *250*, 423.

(19) Jiang, Y. Z.; Song, H. Z.; Li, L.; Bao, W. T.; Meng, G. Y. *J. Cryst. Growth* **2004**, *267*, 256.

(20) Belova, N. V.; Girichev, G. V.; Hinchley, S. L.; Kuzmina, N. P.; Rankin, D. W. H.; Zaitzeva, I. G. *Dalton Trans.* **2004**, 1715.